Microstructure, doping and optical properties of Co2+:ZnAl2O4 transparent ceramics for saturable absorbers: Effect of the ZnF2 sintering additive

Alexander Belyaev, Liza Basyrova, Vadim Sysoev, Maxim Lelet, Stanislav Balabanov, Vladimir Kalganov, Vladimir Mikhailovski, Mikhail Baranov, Evgeniia Stepanidenko, Vladimir Vitkin, et al.

Microstructure, doping and optical properties of Co^{2+}:$ZnAl_2O_4$ transparent ceramics for saturable absorbers: Effect of the ZnF_2 sintering additive

Alexander Belyaev[a,*], Liza Basyrova[b], Vadim Sysoev[c], Maxim Lelet[d], Stanislav Balabanov[a], Vladimir Kalganov[e], Vladimir Mikhailovski[e], Mikhail Baranov[b], Evgeniia Stepanidenko[b], Vladimir Vitkin[b], Olga Dymshits[f], and Pavel Loiko[g]

[a]*G.G. Devyatykh Institute of Chemistry of High-Purity Substances, RAS, 49 Tropinin St., 603951 Nizhny Novgorod, Russia*
[b]*ITMO University, Kronverkskiy pr., 49, 197101 Saint-Petersburg, Russia*
[c]*Lobachevsky State University of Nizhny Novgorod, 23 Gagarin Ave., 603950 Nizhny Novgorod, Russia*
[d]*Research Institute for Chemistry, Lobachevsky State University of Nizhny Novgorod, 23 Gagarin Ave., 603950 Nizhny Novgorod, Russia*
[e]*St. Petersburg State University, 7-9 Universitetskaya Emb., 199034 St. Petersburg, Russia*
[f]*Vavilov State Optical Institute, 36 Babushkina St., 192171 St. Petersburg, Russia*
[g]*Centre de recherche sur les Ions, les Matériaux et la Photonique (CIMAP), UMR 6252 CEA-CNRS-ENSICAEN, Université de Caen Normandie, 6 Boulevard du Maréchal Juin, 14050 Caen Cedex 4, France*

**Corresponding author, e-mail: belyaev@ihps.nnov.ru*

ABSTRACT.

Transparent cobalt-doped zinc aluminate spinel (gahnite), Co^{2+}:$ZnAl_2O_4$, ceramics were fabricated by hot pressing of $(Zn,Co)Al_2O_4$ / ZnF_2 nanopowders at 1520 ºC for 4 hours. A novel approach was suggested for the preparation of $(Zn,Co)Al_2O_4$ precursor: the $(Zn,Co)Al_2O_4$ powders were synthesized by mixing an alcohol solution of aluminium isopropoxide with a joint aqueous solution of zinc *formate* (the source of zinc), cobalt nitrate and zinc fluoride (the sintering additive) followed by drying and calcination in air. The study of the thermal behavior of precursors revealed an optimum calcination temperature (700 ºC) preventing the loss of the sintering additive (ZnF_2). The effect of the ZnF_2 content (3-10 wt%) on the microstructure, the cobalt doping concentration, absorption and luminescence of ceramics was systematically studied. The ceramics exhibit a close-packed microstructure with a mean grain size of 50-70 μm and high in-line transmission (about 84% at ~2 μm). The actual concentration of Co^{2+} ions in tetrahedral (T_d) sites of gahnite is lower than the Co^{2+} doping level and it decreases with the ZnF_2 content. We propose a possible mechanism of this variation including both the losses of Co^{2+} via evaporation of the intermediate CoF_2 phase and a partial location of Co^{2+} ions in octahedral (O_h) sites of gahnite due to its partly inverse spinel structure. The developed ceramics are promising for saturable absorbers of erbium lasers.

Keywords: Transparent ceramics, Hot pressing synthesis, Sintering additive, Gahnite, Cobalt ions, Microstructure, Saturable absorbers of lasers.

1. Introduction

Spinel crystals are complex oxides with a cubic symmetry (sp. gr. $Fd3^{-}m$) having a general chemical formula of AB_2O_4 where A and B are cations with variable valence. Typically, A is a divalent cation, e.g., Mg^{2+}, Fe^{2+}, Zn^{2+} or Mn^{2+} and B is a trivalent one, e.g., Al^{3+} or Fe^{3+} (the so-called 2-3 spinels). A well-known example is $MgAl_2O_4$ [1]. Spinel crystals offer good mechanical and thermal properties and they possess a broad transparency range.

3*d* transition-metal (TM) ions feature partially filled 3*d* orbitals which are not shielded. Their spectroscopic properties determined by transitions of 3*d* electrons are sensitive to the ligand field symmetry and strength. TM ions embedded in tetrahedral (T_d) sites in crystals are attractive because of their broadband linear and nonlinear absorption [2]. The latter arises from the fact that the T_d local field symmetry results in high transition intensities (several orders of magnitude stronger than those for the octahedral (O_h) field). As a result, crystals doped with TM ions entering into the T_d sites are used as saturable absorbers (SAs) of lasers [3-5].

Spinels and, in particular, $MgAl_2O_4$, are attractive for doping with TM ions [6] such as Ni^{2+} [7-10], Co^{2}+ [11], Mn^{2+} [12-16], Fe^{2+} [17-19] or Cr^{3+} [20]. For $MgAl_2O_4$, one example is doping with divalent cobalt (Co^{2+}) ions replacing the Mg^{2+} cations in T_d sites and featuring broad absorption at ~1.5 μm [11]. This absorption spectrally matches the emission of eye-safe erbium lasers. As a result, Co:$MgAl_2O_4$ based crystalline materials have been recognized as SAs of pulsed erbium lasers [21-24] with applications in range-finding, remote sensing (LIDAR), medicine, *etc*.

Zinc aluminate (gahnite) $ZnAl_2O_4$ is another well-known compound in the spinel crystal family [25]. In the mineral form, its color ranges between green, blue, yellow or brown due to the TM ion impurities. Compared to $MgAl_2O_4$, gahnite features better thermal conductivity. E.g., in [26] for ceramic $ZnAl_2O_4$, it was estimated to be ~25 W/mK. $ZnAl_2O_4$ exhibits high mechanical strength (Mohs hardness: 8.0), high thermal and chemical stability and wide band gap (~6 eV). Unfortunately, bulk single crystals of $ZnAl_2O_4$ cannot be obtained by conventional melt growth methods due to dissociation of zinc aluminate at high temperatures close to the melting point (about 1950 °C, depending on the impurities). As an alternative to single crystals, Co:$ZnAl_2O_4$-based transparent glass-ceramics (GCs) [27,28] and Co:$ZnAl_2O_4$ ceramics [29] were proposed.

Polycrystalline transparent ceramics are obtained at temperatures significantly lower than the melting point of corresponding bulk crystals. Their spectroscopic properties resemble those of the crystals. As compared to GCs, they do not contain residual glass phase. The development of cobalt-doped spinel ceramics was manifested by Co:$MgAl_2O_4$ ones [30-35]. Recently, transparent $ZnAl_2O_4$ ceramics were obtained by Goldstein *et al.* by hot isostatic pressing at 1550 °C using hydrothermally synthesized powders [36]. Since then, several studies dedicated to undoped gahnite ceramics [37-40] and only few devoted to Co^{2+}-doped ones

[29] appeared. More recently, Ni^{2+}-doped $ZnAl_2O_4$ transparent ceramics [9] were prepared by melting-vaporing procedure using TeO_2 and Na_2O as melting agents.

One of the limiting factors in the work on obtaining this material is the absence of commercially available powders. The existing methods of synthesis of $ZnAl_2O_4$ powders have certain difficulties. In particular, in the case of simultaneous precipitation of zinc and aluminium nitrates with ammonia solution [41,42], due to formation of complex compounds of zinc with ammonia that are soluble in water, the resulting powder is enriched with aluminium. The same applies to cobalt, which is also coordinated by ammonia, so that it is impossible to control its exact content in the powder. According to literature data, powders synthesized by hydrothermal method [36], decomposition of sulphate salts [37,38], as well as mixing of powders of aluminium and zinc oxides [39,40] were used to fabricate ceramics. Recently, many works on the synthesis of powders have been published, among which are sol-gel synthesis [43], combustion synthesis [44-48], hydrothermal synthesis [14].

Recently, we showed that synthesis the $ZnAl_2O_4$ powders by hydrolyzing alcohol solutions of aluminium isopropoxide with an aqueous solution of zinc acetate [49] is promising for producing transparent ceramics. In this work, we optimize the $ZnAl_2O_4$ powder synthesis by replacing zinc acetate with zinc formate. Zinc formate easily decomposes [50] to form zinc oxide and a mixture of gases, i.e., CO, CO_2, H_2 and H_2O (↑), without formation of carbon residues in the temperature range of 250-300 °C. Other possible option is zinc nitrate. However, nitrate groups contribute to formation of hard particles, which are very difficult to grind in mills of any type. The transition to nitrate forms of metal sources will be possible using automated techniques for obtaining fine precursor powder, e.g., spray drying. Compared to nitrate sources, formate ones make it possible to obtain softer powders. The obtained powders are sintered to produce transparent ceramics by hot pressing in the presence of zinc fluoride (ZnF_2) [51] as a sintering additive. Also in this work, we propose to introduce ZnF_2 directly into the precursor sol, thus excluding an additional step of introduction of the sintering additive at later stages.

In the present paper, we describe the production of Co:$ZnAl_2O_4$ transparent ceramics by hot pressing from powders with different content of cobalt and sintering additive (ZnF_2). We also report on the effect of the sintering additive on microstructure, cobalt doping and spectroscopic properties of ceramics.

2. Experimental

2.1. Thermal evolution of precursor powders

The precursors for production of Co-doped $ZnAl_2O_4$ powders were prepared by hydrolysis of an alcohol solution of aluminium isopropoxide ($Al(OCH(CH_3)_2)_3$), joint aqueous solution of zinc formate ($Zn(CH_2O)_2$) and cobalt nitrate ($Co(NO_3)_2$), as well as aqueous solution of zinc fluoride (ZnF_2). The solubility of ZnF_2 in water is about 15 g/l (at 20 °C). The molar ratio (zinc + cobalt) / aluminium was 1:2. The procedure for the preparation of reagents and

hydrolysis is described in detail in [49]. The resulting precursor was dried in a vacuum box (at a pressure of 60 kPa) under heating up to 250 °C with a rate of 2 °C/min. The dried precursor was grinded in a planetary ball mill and calcined in air in the temperature range of 300 to 900 °C for 20 min. Zinc aluminate powders doped with 0.02 at.% or 0.10 at.% cobalt, and 3, 6 or 10 wt% zinc fluoride were obtained at the optimum temperature of 700 °C for 20 min.

The study of thermal behavior of the precursor and the choice of the heat-treatment regime were carried out by the thermal gravimetric analysis (TGA) and the differential thermal analysis (DTA) using a synchronous TGA / DTA analyzer (model DTG-60H, Shimadzu) in air at a heating rate of 5 °C/min. The phase composition of powders was identified by X-ray diffraction (XRD) using the LabX XRD-6100, Shimadzu diffractometer.

Zinc fluoride has high vapor pressure ($p(ZnF_2)$ = 7 Pa at 775 °C [52], 53 Pa at 855 °C [53]). Calcination of the $Co:ZnAl_2O_4/ZnF_2$ precursor at high temperatures may lead to a significant loss of the sintering additive. To avoid this, a thermal gravimetric study of decomposition of the precursor was carried out. The TGA / DTA data of the 0.1 at.% $Co:ZnAl_2O_4$ / 6 wt% ZnF_2 dried precursor are shown in Fig. 1. The mass loss (about 7 wt%) at the temperatures up to 200 °C accompanying an endothermic peak (105 °C) corresponds to the removal of water. A small exothermic peak at ~245 °C may correspond to oxidation of formate groups by atmospheric oxygen and oxidation initiated by NO_3^- groups. The significant mass loss of ~25 wt% between 220 °C and 300 °C accompanying an endothermic peak (276 °C) corresponds to decomposition of formate groups. Further mass losses (5 %) starting at above 500 °C correspond to evaporation of the sintering additive of ZnF_2 (melting point: 872 °C) and removal of hydroxyl groups. Thus, significant losses comparable to the content of the sintering additive can be explained by the predominant evaporation of ZnF_2. An exothermic peak at 850 °C corresponds the crystallization of zinc aluminate. The reason for the appearance of an exothermic peak with a maximum of 585 °C is not entirely understandable. Most likely, it is associated with the formation of intermediate fluorine-containing compounds because an exothermic peak at 585 °C was not observed on the TGA / DTA curve of the precursor without zinc fluoride, according to [49] and the laboratory protocol. To decrease the unwanted loss of the sintering additive, the powders should be calcined at the lowest possible temperature for the shortest possible time. The use of zinc in the formate form allowed us to decrease the temperature and time of powder calcination, as high temperatures are not required for removal of organic residues.

Fig. 2 shows XRD patterns of powders calcined at the temperatures in the range of 300–900 °C for 20 min. Gahnite crystallization begins at 500 °C, as confirmed by the appearance of weak and broad diffraction peaks. The calcination at 900 °C gives a significant increase in the crystal size and crystallinity of the powder, as indicated by notably narrowed diffraction peaks increased in intensity. The mean size of crystallites in the powders calcined at 700 °C and 900 °C was estimated using the Scherrer's equation [54] to be 8 nm and 37 nm, respectively. The crystallization of zinc aluminate at 500 ºC and 700 °C occurs by a solid-

phase reaction, and at 900 °C - by dissolving and re-precipitation in the in the $ZnAl_2O_4$ / ZnF_2 eutectic melt. It should be noted that the XRD patterns of calcined powders do not contain reflexes of ZnF_2. The mass loss of the Co:$ZnAl_2O_4$ / ZnF_2 precursor at above 700 °C observed during the TGA / DTA analysis (Fig. 1) is undesirable, so that the heat treatment of the powders at 700 °C is preferable.

Note that weak reflexes of zinc oxide (ZnO) are present in the XRD pattern of powder calcined at 900 °C. The impurity phase of ZnO may indicate that the crystallization of zinc aluminate has not been completed, but will be completed at hot pressing of ceramics. Note that these powders were not used for the synthesis of ceramics in the present work. If calcination of powders at higher temperatures would be required, the initial batch should be enriched in aluminium if the powder stoichiometry is shifted to zinc.

2.2. Fabrication of ceramics

To fabricate transparent ceramics, synthesized powders were hot pressed in a home-made machine at a temperature of 1520 °C for 4 h. The powders were pressed under 50 MPa in a steel mold (diameter: 15 mm) and placed into a graphite mold. The hot pressing included the following stages: (i) heating up to 950 °C with a constant pressure of 3 MPa, (ii) first dwell for 10 min with a constant pressure, (iii) heating up to 1200 °C with a gradual pressure rise up to 40 MPa, (iv) second dwell for 20 min with a constant pressure, (v) heating up to 1520 °C, (vi) final dwell for 4 h, (vii) free cooling. Sintering of ceramics was carried out in a vacuum atmosphere.

The general mechanism of action the sintering additive for liquid-assisted-sintering (ZnF_2, in our case) includes (i) its role as a lubricant that promotes sliding of particles during shrinkage, (ii) recrystallization in the melt due to dissolution of small particles and precipitation on large particles and (iii) formation of sintering additive-associated vacancies that facilitate sintering at later stages of the sintering process.

The ceramic disks (thickness: 2 mm, diameter: 15 mm) were polished to laser-grade quality from both sides. They were transparent, Fig. 3, and had a blue coloration due to the cobalt doping. For a fixed Co content in the initial powders, the coloration decreased with increasing the ZnF_2 content (see below).

For spectroscopic studies, half of the ceramic disk was additionally annealed at 1400 °C for 30 min in air to eliminate the possible oxygen vacancies.

2.3. Characterization of ceramics

The X-ray powder diffraction (XRD) patterns of ceramic samples were recorded using a Shimadzu XRD-6000 diffractometer, Cu Kα radiation (1.54060 Å) with a Ni filter. The lattice constant *a* for ceramics was determined by Rietveld refinement.

The microstructure of a clean fracture surface of ceramic disks was studied using a scanning electron microscope (SEM, MERLIN, Carl Zeiss). The size distribution of grains

was analyzed by manual counting using ImageJ software. The composition of ceramics was studied by Energy Dispersive X-ray (EDX) spectroscopy. For this, we used a similar electron microscope (accelerating voltage: 20 kV, beam current: 2 nA) equipped with an INCA X-Act (Oxford Instruments) microanalyzer. To avoid the unwanted charging of the dielectric ceramic surface, it was coated with a thin (thickness: 10 nm) carbon film prior to SEM studies.

All spectroscopic studies were performed at room temperature (20 °C). The transmission spectra were measured with a Shimadzu UV 3600 spectrophotometer (0.3–2 μm). The Raman spectra and the luminescence were detected using a confocal Raman microscope (inVia, Renishaw) equipped using a Leica ×50 objective (N.A. = 0.75). The excitation wavelength λ_{exc} was 514 nm (Ar^+ laser line).

The luminescence decay was studied using a time-resolved confocal fluorescence microscope equipped with a ×100 objective (N.A. = 0.95) (MicroTime 100, PicoQuant). As the excitation source, a picosecond (ps) diode laser emitting at 405 nm was used.

3. Results and discussion

3.1. Microstructure

The structure and the phase purity of ceramics were confirmed by X-ray powder diffraction, Fig. 4. The measured XRD patterns correspond to that of undoped $ZnAl_2O_4$ (according to the ICSD (Inorganic Crystal Structure Database) card #9559) [55]. Co:$ZnAl_2O_4$ is cubic (sp. gr. O^7_h – $Fd\bar{3}m$, #227). The lattice constant a for ceramics was weakly dependent on the ZnF_2 content. For ceramic prepared from powders containing 0.1 at.% Co and 10 wt% ZnF_2, a = 8.088 Å.

A similar microstructure was observed for all studied ceramics. The example SEM images of a fracture surface of ceramics prepared from powders containing 0.1 at.% Co and 3 / 10 wt.% ZnF_2 are shown in Fig. 5(a,b). The ceramics exhibit a close-packed structure with clean grain boundaries and a lack of μm-sized pores. The mean grain size was determined by counting about 100 crystallites for each sample. The measured linear dimensions of grains were multiplied by a shape factor of 1.2 (accounting for slight deviations from the spherical shape). Fig. 6(a) shows the grain size distribution for the series of ceramics prepared from powders doped with 0.02 at.% Co and 3–10 wt% ZnF_2. For all samples, a relatively broad range of grain sizes (20–100 μm) was observed revealing a dependence on the position in the ceramic disk: larger grains in the central part and smaller grains at the perimeter of the disk.

The effect of the ZnF_2 content on the mean grain size D_{grain} is shown in Fig. 6(b). For 0.02 at.% Co doping, with increasing the amount of the sintering aid, first, D_{grain} slightly increases (from 55 μm for 3 wt% ZnF_2 to 68 μm for 6 wt% ZnF_2) and then decreases to 60 μm for 10 wt% ZnF_2. A similar tendency is observed for 0.1 at.% Co doping. These values are larger than those observed in an undoped $ZnAl_2O_4$ ceramics (D_{grain} = 40 μm, using the same shape factor) produced by a similar method with 5 wt% ZnF_2 [51]. The observed trends for

the variation of the grain size may be masked by the relatively broad grain size distribution observed in the studied ceramics; therefore, it is difficult to draw conclusions in this relation.

The composition of ceramics was studied by EDX. The presence of fluorine was detected in all the studied samples. The concentration of F^- ions in ceramics slowly increased with the ZnF_2 content in the precursor powders. We assume that the F^- ions may be diffusely distributed at the grain boundaries or dissolved in the grains. The EDX spectra of ceramics prepared from powders containing 0.1 at.% Co and 3-10 wt% ZnF_2 are shown in Fig. 7. The element mapping (Al, Zn, O, Co and F) obtained by the means of EDX is shown in Fig. 8.

3.2. Raman spectra

The structure of ceramics was confirmed by Raman spectroscopy, Fig. 9. According to the group-theory analysis, the irreducible representations at the Γ point (***k*** = 0) of the Brillouin zone are as following: $\Gamma = A_{1g} + E_g + T_{1g} + 3T_{2g} + 2A_{2u} + 2E_u + 5T_{1u} + 2T_{2u}$ [56]. Five modes (A_{1g}, E_g and $3T_{2g}$) are Raman-active, five ($5T_{1u}$) are IR-active and other are acoustic or silent. In the Raman spectra of ceramics, all five modes are observed at 195 cm^{-1} (T_{2g}), 417 cm^{-1} (E_g), ~510 cm^{-1} (T_{2g}), 657 cm^{-1} (T_{2g}) and ~800 cm^{-1} (A_{1g}). The spectra are weakly dependent on the starting composition. The two most intense modes are due to the motion of Al and O atoms [57].

A careful inspection of the Raman spectra did not reveal characteristic vibrations of possible fluoride phases (CoF_2 or ZnF_2) and ZnO. In particular, for CoF_2, these are 68, 246, 366 and 494 cm^{-1} [58] and for and for ZnF_2 – 70, 253, 350 and 522 cm^{-1} [59]. For ZnO, the characteristic Raman bands are at 99, 333 and 438 cm^{-1} [60].

3.3. Optical absorption

The in-line transmission (*T*) spectra of polished ceramic disks are shown in Fig. 10(a). First, let us discuss the transmission at 1.9 μm (out of cobalt absorption bands). Depending on the composition of the precursor, it amounts to *T* = 83.2%-84.0%, which is close to the theoretical value set by Fresnel losses, T_0 = 84.3%, assuming a refractive index *n* of 1.80 [61]. High transmission indicates good optical quality of ceramics. For the increased cobalt concentration in the precursor, the transmission slightly decreases. However, we did not observe a direct relation between transmission and the ZnF_2 content.

The observed spectral bands are due to absorption of Co^{2+} ions in tetrahedral sites in the spinel structure. The Co^{2+} ion has the electronic configuration of $[Ar]3d^7$. The ground-state is $^4A_2(^4F)$, so that the spin-allowed transitions occur to quartet states, ^4F and ^4P. However, the transition to the lower-lying excited-state $^4T_2(^4F)$ is forbidden in an undistorted T_d ligand field, so it has a small oscillator strength [11] and it is observed as a weak band at ~2.55 μm. The intense and broad (1.06–1.64 μm) absorption band with local peaks at 1248, 1297, 1428, and 1503 nm corresponds to transitions to the $^4T_1(^4F)$ state. The second intense band in the visible (0.50–0.68 μm) with local peak at 547, 587 and 620 nm corresponds to transitions to

the $^4T_1(^4P)$ state. The local peaks in both bands are related to the spin-orbit splitting of the quartet states [30]. For example, for the $^4T_1(^4F)$ state of tetrahedral Co^{2+} ions in gahnite, the previously determined energies of the spin-orbit splitted sub-levels of $^4T_1(^4P)$ at 4.2 K are 6756(Γ_6), 7072(Γ_8), 7776(Γ_7) and 7850(Γ_8) cm^{-1} [25], corresponding to the wavelengths in absorption of 1480, 1414, 1286 and 1273 nm, respectively. For the studied ceramics, the positions of sub-levels may slightly vary as compared to the single-crystal.

Besides the spin-allowed transitions, the spectra contain weak bands assigned to transitions to the higher-lying splitted ^2G, ^2P and ^2H doublet excited-states. In particular, the transitions to the ^2E, $^2T_1$, $^2A_1$ and $^2T_2(^2G)$ excited-states (in an increasing energy order) contribute to intense absorption band in the visible. At shorter wavelengths (<0.50 μm), weak structured absorption is due to transition to the $^2T_1(^2P)$, $^2T_2$, $^2T_1$, ^2E and $^2T_1(^2H)$ excited-states (in an increasing energy order). Here, the assignment is according to the energy levels reported in [25,62]. More details about the crystal-field of tetrahedral Co^{2+} ions in gahnite can be found elsewhere [63]. Weak and broadband absorption at these wavelengths may also originate from Co^{2+} ions in octahedral sites [64] (see Section 4.4).

A detailed view on visible absorption of an example ceramic sample made of powders doped with 0.1 at.% Co and 3 wt% ZnF_2 is given in Fig. 10(b). The bands at 477 nm, ~445 nm and 406 nm are assigned to transitions to the $^2T_1(^2P)$, $^2T_2$ and $^2T_1(^2H)$ states, respectively. Other transitions to the ^2H doublet states are not visible because of their weak intensity. For the as-sintered ceramic, a broad absorption band at ~275 nm is observed overlapping with the UV absorption edge (λ_{UV} = 245 nm, optical bandgap E_g: ~5.5 eV). After annealing, the Co^{2+} absorption features do not change implying that new Co^{2+} sites with T_d symmetry are not formed, while the intensity of the UV band increases significantly thus shifting the absorption edge to λ_{UV} = 292 nm. In the previously studied undoped $ZnAl_2O_4$ ceramics sintered with 5 wt% ZnF_2 [49], no such absorption was detected resulting in E_g = 6.05 eV. In the present work, sintering of ceramics was carried out in a vacuum atmosphere, which may lead to formation of oxygen vacancies. Oxidative annealing contributes to the drain of vacancies (see Section 4.5) with formation of pores of nm and sub-μm size leading to additional light scattering and a red-shift of the UV absorption edge of the material.

The scheme of energy levels of tetrahedral Co^{2+} ions can be analyzed within the equivalent Tanabe-Sugano diagram [65] for the d^3 complexes in octahedral field, Fig. 11(a). Here, we omit the "g" subscripts because all the states are even (*gerade*). The Co^{2+} absorption in the $ZnAl_2O_4$ matrix corresponds to the region of the diagram where the branches corresponding to the ^4P and ^2G states intersect. As a result, the doublet states ^2E and $^2T_1(^2G)$ are lying below the quartet $^4T_1(^4P)$ one, as shown in Fig. 11(b) according to the crystal-field splitting from [25]. As compared to Co:$MgAl_2O_4$ [66], gahnite shows smaller splitting of the $^4T_1(^4F)$ and $^4T_1(^4P)$ states.

3.4. Cobalt doping

A general chemical formula for spinels is AB_2O_4 (cubic system, sp. gr. $Fd\bar{3}m$). Each unit cell contains 32 anions (O^{2-}) in a face-centered cubic packing. Inside the oxygen lattice, the cations (A^{2+} and B^{3+}) have 32 octahedral (O_h) and 64 tetrahedral (T_d) available interstitial sites per unit cell. In a normal spinel structure, 1/8 of the T_d sites are occupied by divalent cations A^{2+} and 1/2 of the O_h sites are occupied by trivalent cations B^{3+}. Spinels can demonstrate a certain degree of cation disorder. It is described by an inversion parameter δ which is a fraction of B^{3+} cations in the T_d sites (or, equivalently, a fraction of A^{2+} cations in the O_h sites). As a result, the formula for spinels may be written as $^{IV}[A_{1-\delta}B_\delta]^{VI}[B_{2-\delta}A_\delta]O_4$. The spinel is normal for $\delta = 0$ and inverse for $\delta = 1$. For $\delta = 2/3$, cations have a completely random distribution over the T_d and O_h sites [63].

In the case of gahnite, this formula is $^{IV}[Zn_{1-\delta}Al_\delta]^{VI}[Al_{2-\delta}Zn_\delta]O_4$. Here, the superscripts are the coordination numbers (C.N. = IV and VI for the T_d and O_h sites, respectively). The Co^{2+} ions in the spinel structure are expected to replace the Zn^{2+} ones. In this way, some part of Co^{2+} ions may be located in octahedral sites [63,67]. Because a center of symmetry is present for the O_h site, the intensity of transitions for $^{VI}Co^{2+}$ ions will be several orders of magnitude weaker as compared to the $^{IV}Co^{2+}$ ones [25]. Thus, the former species will contribute to absorption with much lower intensity.

It is known that $Co:ZnAl_2O_4$ exhibits a notable inversion, depending on the size of the crystallites and Co^{2+} concentration. With increasing the Co^{2+} doping level reaching the stoichiometric composition of cobalt aluminate ($CoAl_2O_4$), δ increases [67]. It was also shown that the inversion parameter decreases with increasing the crystallite size [64]. However, the presence of a notable fraction of octahedral Co^{2+} ions in bulk gahnite crystals was also claimed [25].

It is known that the lattice constant of Co^{2+}-doped $ZnAl_2O_4$ is an indication of a degree of inversion. For an undoped $ZnAl_2O_4$ ceramics studied for comparison, we have determined $a = 8.087$ Å which is a typical value for undoped synthetic gahnite [68]. The assumption that Co^{2+} ions are entering into the spinel structure solely in T_d sites should lead to a decrease of a. Indeed, for a C.N. = IV, the ionic radii of Co^{2+} and Zn^{2+} are 0.58 Å and 0.60 Å, respectively [69]. In [67], it was suggested that the main reason for increasing a is the intersite-cation exchange (quantified by increasing δ parameter), namely, Co^{2+} for Al^{3+} substitution on the O_h sites. Indeed, the corresponding ionic radii of Co^{2+} and Al^{3+} for C.N. = VI are 0.745 Å and 0.535 Å [69].

Now, let us analyze the broad absorption band due to the $^4A_2(^4F) \rightarrow {}^4T_1(^4F)$ transition of $^{IV}Co^{2+}$ ions, Fig. 12(a). For a fixed concentration of Co^{2+} in the precursor, the absorption coefficient (α_{abs}) decreases linearly with increasing the ZnF_2 content, e.g., as shown in Fig. 12(b) for the reference wavelength of 1.54 μm. Moreover, even extrapolation of the $\alpha_{abs}(ZnF_2)$ dependence to the limit of absent sintering additive gives a lower value of the absorption coefficient than the expected one, $\alpha_{abs0} = \sigma_{GSA} \cdot N_{Co0}$. Here, σ_{GSA} is the ground-state absorption (GSA) cross-section of Co^{2+} ions in T_d sites, N_{Co0} is the Co^{2+} concentration assum-

ing that all cobalt ions enter into the ceramic grains. For the initial concentrations of 0.02 at.% and 0.1 at.% Co, $N_{Co0} = 0.303\times10^{19}$ cm^{-3} and 1.515×10^{19} cm^{-3}, respectively (as calculated assuming the density of ceramics ρ = 4.61 g/cm^3). Previously, for transparent GCs based on Co:$ZnAl_2O_4$ nanocrystals, σ_{GSA} at 1.54 μm was determined to be 2.0×10^{-19} cm^2 [27] and 2.45×10^{-19} cm^2 (used in the present work) [30] being lower than that for the Co:$MgAl_2O_4$ single-crystal, 3.5×10^{-19} cm^2 [3]. A similar analysis can be performed based on the visible absorption band of Co^{2+} ions. In particular for $ZnAl_2O_4$, it is complicated by the lack of reliable data on the GSA cross-sections for the $^4A_2(^4F) \rightarrow {}^4T_1(^4P)$ transition.

From the measured absorption coefficient α_{abs} at 1.54 μm, we estimated the actual concentration of Co^{2+} ions in T_d sites $N_{Co}(T_d) = \alpha_{abs}/\sigma_{GSA}$ (Table 1). It decreases linearly with the ZnF_2 content and it is about 2 times lower than the N_{Co0} value. There can exist two reasons for this. One is the presence of a fraction of Co^{2+} ion in O_h sites (as described above) that does not contribute to linear absorption at ~1.54 μm. A similar mechanism was proposed previously for Co:$ZnAl_2O_4$-based transparent glass-ceramics to explain their non-saturable losses [28]. However, as all the studied ceramics are synthesized under the same conditions, this fraction is expected to be nearly independent of the ZnF_2 content. Consequently, another reason is a chemical process involving ZnF_2 and occurring during sintering of ceramics.

Let us describe the role of ZnF_2. We suppose that cobalt (II) fluoride (CoF_2) is the key intermediate of the sintering process. CoF_2 can be formed both at the stage of precursor synthesis and during the sintering itself (through an interaction of ZnF_2 and AlF_3 (if it is formed during the evolution of a precursor or during the sintering) with cobalt ions within the green body), according to the following reactions:

$Co^{2+} + 2F \rightarrow CoF_2\downarrow$,

$ZnF_2 + Co^{2+} \rightarrow CoF_2 + Zn^{2+}$,

$2AlF_3 + 3Co^{2+} \rightarrow 3CoF_2 + 2Al^{3+}$,

respectively.

The formed CoF_2 is less volatile (~12 Pa at 950 °C [70]) than ZnF_2 (~458 Pa at 950 °C, extrapolated from [53]) and AlF_3 (~ 395 Pa at 950 °C [71]), hence, it is removed later (at higher temperatures). Indeed, the melting points of ZnF_2 and CoF_2 are 872 °C and ~1200 °C, respectively. CoF_2 may be removed by evaporation and / or sublimation. The AlF_3 vapor pressure is lower than that of ZnF_2 but of the same order; therefore, sintered ceramics can be slightly enriched with zinc (see Fig. 2, 900 °C), as AlF_3 can also evaporate. The following equations describe the process of regeneration of spinel lattice according to the reverse exchange reactions ((l) and (s) stand for liquid and solid phases, respectively):

$CoF_2(s) + Zn^{2+} \rightarrow ZnF_2\uparrow + Co^{2+}$,

$CoF_2(l) + Zn^{2+} \rightarrow ZnF_2\uparrow + Co^{2+}$.

If the rate of these processes is less than the rate of evaporation / sublimation of CoF_2, the actual Co^{2+} concentration in the ceramics will decrease. Here, CoF_2(l) is a melt. The melting point of CoF_2 is ~1200 °C and during the hot pressing, cobalt fluoride which has not been

evaporated yet, will be completely liquid. In more details, taking into account the thermodynamic approach, similar processes are considered for the $MgAl_2O_4$ / LiF system in [72].

Separately, it is worth noting that there is a possibility of presence of diffusely distributed CoF_2 at the grain boundaries as a residue, because fluorine is found in ceramics at the level of the detection limit (Section 4.1). However, this option does not change the model of probable formation of CoF_2.

Note that we did not use $Co:ZnAl_2O_4$ ceramics fabricated without the sintering aid for the analysis in Fig. 12(b) as they were translucent and it was impossible to quantify the Co^{2+} absorption.

To conclude, the reduction in Co^{2+} concentration in T_d sites with respect to the value obtained when extrapolating the $\alpha_{abs}(ZnF_2)$ dependence to the limit of no sintering aid is due to the ZnF_2-assisted evaporation of cobalt in the form of CoF_2. The residual difference in concentrations (45% for 0.1 at.% Co and 28% for 0.02 at.% Co) is ascribed to the inverse spinel structure (predominantly) and losses of cobalt not related to ZnF_2. Indeed, cobalt may also reduce to the metallic form with the zero oxidation state (e.g., due to the reaction with CO gas or graphite). This will however lead to formation of pores and translucent character of ceramics which is not observed in our case. It should be also noted that oxidative annealing would lead to the oxidation of metallic cobalt and the entry of Co^{2+} into the spinel lattice, as well as to an increase in the intensity of cobalt absorption bands. However, it is not noted (see Fig. 10(b)). Thus, this mechanism seems to play a minor role.

3.5. Luminescence

The luminescence spectra of as-sintered $Co:ZnAl_2O_4$ ceramics are shown in Fig. 13(a). The spectra contain an intense band centered at ~645 nm (emission bandwidth: 43 nm) and a weak and broad band centered at ~860 nm both ascribed to Co^{2+} ions in T_d sites. The spin-allowed transitions in emission occur from the $^4T_1(^4P)$ state to the $^4A_2(^4F)$ and $^4T_2(^4F)$ ones, respectively. As mentioned above, the doublet states ^2E and $^2T_1(^2G)$ in $Co:ZnAl_2O_4$ are lying below the $^4T_1(^4P)$ state while their populations are thermalized at room-temperature. Thus, $^2E(^2G)$ is the emitting state.

With the increase of the actual Co^{2+} concentration in T_d sites (cf. Table 1), or, equivalently, with the decrease of the ZnF_2 content in the precursor powders, the luminescence intensity gradually increases while no significant change of the spectral shape is observed. No concentration-quenching is observed up to at least 0.050 at.% Co in T_d sites (actual).

We have monitored the effect of annealing on the emission properties of ceramics, see Fig. 13(b). After annealing, the intensity of luminescence related to Co^{2+} ions in T_d sites notably increases while the emission ascribed to defects is suppressed. This is because annealing efficiently removes oxygen vacancies leading to better crystallinity of the material.

Other spectral features are the sharp emission lines at 676–723 nm and a weak and broad emission centered at ~740 nm, Fig. 13(c). Previously, we demonstrated [29] that gahn-

ite ceramics contains chromium (Cr^{3+}) impurity ions that come with ZnO raw material. The sharp emission lines at 676–723 nm are due to Cr^{3+}ions substituting the Al^{3+} cations in O_h sites (the so-called N-lines) [73,74]. The broad emission centered at ~740 nm is assigned to the structure defects [75,76]. In particular, the transitions from the conduction band (CB) or shallow donor defect states (e.g., Al^*_{Zn} – aluminium antisite defects) to deep donor defect states (V^*_O – oxygen vacancies) may explain this emission.

The luminescence decay was studies for the as-sintered ceramic samples. When exciting the samples at 405 nm and detecting luminescence in the whole visible spectral range, the measured luminescence decay curves exhibited intense "fast" time component (decay time: τ_{fast} = 3.0±0.2 ns, being weakly dependent on composition of the starting powders) assigned to emission of defects, and much weaker "slow" component (τ_{slow} ~ hundreds of ns) attributed to emission of Co^{2+} ions. Indeed, by spectral filtering only the emission band at ~645 nm, see Fig. 13(a), we observed predominantly the latter decay. The luminescence decay curves were well fitted with a single-exponential law, Fig. 14. For ceramics obtained from powders doped with 0.1 at.% Co, the determined decay time τ_{slow} decreased in the range 272–222 ns for the ZnF_2 content decreasing from 10 to 3 wt% (or, equivalently, with increasing concentration of Co^{2+} ions in T_d sites). The τ_{slow} value has a meaning of the lifetime of the $^2E(^2G)$ Co^{2+} state. Our observations agree well with the previous studied of Co:$ZnAl_2O_4$-based GCs [27,28]: it was determined that the lifetime of the $^2E(^2G)$ excited-state of Co^{2+} ions in T_d sites decreases from 200 to 25 ns for increasing the concentration of CoO in the initial glass (0.1–2 wt%).

As a final remark, one may point out the cost effectiveness and simplicity of synthesis of Co^{2+}-doped $ZnAl_2O_4$ nanopowders and transparent ceramics in the present work. This is in line with the recent studies [77,78] focusing on similar materials.

4. Conclusions

We report on fabrication of a series of highly transparent cobalt-doped zinc aluminate spinel (gahnite) ceramics – Co^{2+}:$ZnAl_2O_4$. For this, we employed a modified approach with the following features: (i) an original way of fabrication of the precursor nanopowders by using zinc *formate* as a source of zinc and an aqueous solution of zinc fluoride as a sintering additive. The first detail allowed us to reduce the temperature and time of calcination of powders (as formate easily decomposes at 250–300 °C) without carbonization of the powder (formate does not contain C–C bonds). The second detail is the preparation of the precursor using solutions of metal sources *together* with an aqueous solution of the sintering additive (ZnF_2), which eliminates the need for additional steps for its introduction at later stages. Such principles have never been used before for $ZnAl_2O_4$ transparent ceramics; (ii) an optimum temperature of powder calcination (700 ºC) determined from thermal studies and reducing losses of the sintering additive (ZnF_2), (iii) the particular temperature of hot-pressing (1520 °C) to produce transparent ceramics. With this improved chemical way, we obtained ceram-

ics with excellent transparency close to the theoretical limit and suitable microstructure (relatively small grains, clear grain boundaries and the lack of μm-sized pores).

We determined that the concentration of Co^{2+} ions in T_d sites in the ceramic specimens is lower than the initial concentration in the precursor powders and, furthermore, it decreases with the ZnF_2 content. This is ascribed to two main reasons: (i) accommodation of Co^{2+} ions in octahedral sites (inversion of spinel structure) and the loss of Co^{2+} via evaporation of an intermediate phase of CoF_2. A linear variation of the tetrahedral Co^{2+} concentration with the ZnF_2 content allowed us to control precisely the absorption at around ~1.5 μm (the $^4A_2(^4F) \rightarrow {}^4T_1(^4F)$ transition of $^{IV}Co^{2+}$ ions) without deterioration of optical quality of ceramics. The latter is of practical importance for development of ceramic saturable absorbers for eye-safe erbium lasers. Further efforts should be applied on revealing the effect of octahedral Co^{2+} ions on nonlinear properties of $Co:ZnAl_2O_4$ ceramics (e.g., via non-saturable losses).

Acknowledgements

This study was funded by RFBR (Russian Foundation for Basic Research, Russia) according to the research project No. 18-33-00152 and by Russian Science Foundation (Agreement No. 18-13-00200). The study of thermal evolution of the precursor and its phase purity was carried out on the equipment of the Collective Usage Center "New Materials and Resource-saving Technologies" (Lobachevsky State University of Nizhny Novgorod, Russia). O.D. acknowledges partial financial support from RFBR (Project No. 19-03-00855). EDX studies were performed at Interdisciplinary Resource Center for Nanotechnology of Research Park of Saint-Petersburg University.

References

[1] I. Ganesh, A review on magnesium aluminate ($MgAl_2O_4$) spinel: synthesis, processing and applications, Intern. Mater. Rev. 58 (2013) 63-112.

[2] A.M. Malyarevich, K.V. Yumashev, Saturable absorbers based on tetrahedrally coordinated transition-metal ions in crystals, J. Appl. Spectr. 76 (2009) 1-43.

[3] K.V. Yumashev, I.A. Denisov, N.N. Posnov, P.V. Prokoshin, V.P. Mikhailov, Nonlinear absorption properties of $Co^{2+}:MgAl_2O_4$ crystal, Appl. Phys. B 70 (2000) 179–184.

[4] T.Y. Tsai, M. Birnbaum, Co^{2+}:ZnS and Co^{2+}:ZnSe saturable absorber Q switches, J. Appl. Phys. 87 (2000) 25-29.

[5] K.V. Yumashev, I.A. Denisov, N.N. Posnov, N.V. Kuleshov, R. Moncorge, Excited state absorption and passive Q-switch performance of Co^{2+} doped oxide crystals, J. Alloys Compd. 341 (2002) 366-370.

[6] K. Izumi, S. Miyazaki, S. Yoshida, T. Mizokawa, E. Hanamura, Optical properties of 3*d* transition-metal-doped $MgAl_2O_4$ spinels, Phys. Rev. B 76 (2007) 075111.

[7] N.V. Kuleshov, V.G. Shcherbitsky, V.P. Mikhailov, S. Kück, J. Koetke, K. Petermann, G. Huber, Spectroscopy and excited-state absorption of Ni^{2+}-doped $MgAl_2O_4$, J. Lumin. 71 (1997) 265-268.
[8] A. Saleem, Y. Zhang, H. Gong, M. K. Majeed, J. Jing, X. Lin, J. Mao, M. Z. Ashfaq, Structural, magnetic and dielectric properties of nano-crystalline spinel $Ni_xCu_{1-x}Fe_2O_4$, J. Alloys Compd. 825 (2020) 154017.
[9] G. Yu, W. Wang, C. Jiang, A facile approach towards fabrication and ultrabroad band emission properties of nickel ion-doped $ZnAl_2O_4$ transparent ceramics, Ceram. Intern., doi: 10.1016/j.ceramint.2020.01.026 (2020).
[10] J. Wang, A. Wang, D. Hu, X. Wu, Y. Liu, T. Chen, Synthesis, characterization and properties of Ni^{2+}-doped $ZnAl_2O_4$-based spinel-type solid acid catalysts: $SO4^{2-}/Zn_{1-x}Ni_xAl_2O_4$, Mater. Chem. Phys. 239 (2020) 122319.
[11] N.V. Kuleshov, V.P. Mikhailov, V.G. Scherbitsky, P.V. Prokoshin, K.V. Yumashev, Absorption and luminescence of tetrahedral Co^{2+} ion in $MgAl_2O_4$, J. Lumin. 55 (1993) 265-269.
[12] E. Song, X. Jiang, Y. Zhou, Z. Lin, S. Ye, Z. Xia, and Q. Zhang, Heavy Mn^{2+} doped $MgAl_2O_4$ phosphor for high-efficient near-infrared light-emitting diode and the night-vision application, Adv. Opt. Mater. 7 (2019) 1901105.
[13] A. Tomita, T. Sato, K. Tanaka, Y. Kawabe, M. Shirai, K. Tanaka, E. Hanamura, Luminescence channels of manganese-doped spinel, J. Lumin. 109 (2004) 19-24.
[14] S. Huang, Z. Wei, X. Wu, J. Shi, Optical properties and theoretical study of Mn doped $ZnAl_2O_4$ nanoparticles with spinel structure, J. Alloys Compd. 825 (2000) 154004.
[15] A. Ashok, L.J. Kennedy, J.J. Vijaya, Structural, optical and magnetic properties of $Zn_{1-x}Mn_xFe_2O_4$ ($0 \leq x \leq 0.5$) spinel nano particles for transesterification of used cooking oil, J. Alloys Compd. 780 (2019) 816-828.
[16] E.H. Song, Y.Y. Zhou, Y. Wei, X.X. Han, Z.R. Tao, R.L. Qiu, Z.G. Xia, Q.Y. Zhang, A thermally stable narrow-band green-emitting phosphor $MgAl_2O_4$:Mn^{2+} for wide color gamut backlight display application, J. Mater. Chem. C 7 (2019) 8192-8198.
[17] A.A. El-Fadl, M.I. Abd-Elrahman, N. Younis, N. Afify, A.A. Abu-Sehly, M.M. Hafiz, Syntheses of new spinels $Zn_{1-x}Fe_xAl_2O_4$ nanocrystallines structure: Optical and magnetic characteristics, J. Alloys Compd. 795 (2019) 114-119.
[18] L. Basyrova, S. Balabanov, A. Belyaev, V. Drobotenko, A. Volokitina, V. Vitkin, O. Dymshits, P. Loiko, Synthesis, structure and spectroscopy of Fe^{2+}:$MgAl_2O_4$ transparent ceramics, J. Phys.: Conf. Series 1410 (2019) 012123.
[19] V.V. Osipov, V.A. Shitov, R.N. Maksimov, K.E. Lukyashin, V.I. Solomonov, A.V. Ishchenko, Fabrication and characterization of IR-transparent Fe^{2+} doped $MgAl_2O_4$ ceramics, J. Amer. Ceram. Soc. 102 (2019) 4757-4764.

[20] Feofilov, S.P., Kulinkin, A.B., Kaveev, A.K., Sokolov, N.S. and Suturin, S.M., 2020. Fluorescence of Cr^{3+} ions in $MgAl_2O_4$ epitaxial nanosize spinel films on $SrTiO_3$ substrates, Thin Solid Films 693 (2020) 137732.
[21] G. Karlsson, V. Pasiskevicius, F. Laurell, J.A. Tellefsen, B. Denker, B.I. Galagan, V.V. Osiko, S. Sverchkov, Diode-pumped Er–Yb:glass laser passively Q switched by use of Co^{2+}:$MgAl_2O_4$ as a saturable absorber, Appl. Opt. 39 (2000) 6188-6192.
[22] K.N. Gorbachenya, V.E. Kisel, A.S. Yasukevich, V.V. Maltsev, N.I. Leonyuk, N.V. Kuleshov, Eye-safe 1.55 μm passively Q-switched Er,Yb:$GdAl_3(BO_3)_4$ diode-pumped laser, Opt. Lett. 41 (2016) 918-921.
[23] P.A. Loiko, O.S. Dymshits, N.A. Skoptsov, A.M. Malyarevich, A.A. Zhilin, I.P. Alekseeva, M.Y. Tsenter, K.V. Bogdanov, X. Mateos, K.V. Yumashev, Crystallization and nonlinear optical properties of transparent glass-ceramics with Co:$Mg(Al,Ga)_2O_4$ nanocrystals for saturable absorbers of lasers at 1.6–1.7 μm, J. Phys. Chem. Sol. 103 (2017) 132-141.
[24] V. Vitkin, P. Loiko, O. Dymshits, A. Zhilin, I. Alekseeva, D. Sabitova, A. Polishchuk, A. Malyarevich, X. Mateos, and K. Yumashev, Passive Q-switching of an Er, Yb:glass laser with Co:$Mg(Al,Ga)_2O_4$-based glass-ceramics, Appl. Opt. 56 (2017) 2142-2149.
[25] J. Ferguson, D.L. Wood, L.G. Van Uitert, Crystal-field spectra of $d^{3,7}$ Ions. V. Tetrahedral Co^{2+} in $ZnAl_2O_4$ spinel, J. Chem. Phys. 51 (1969) 2904-2910.
[26] N.J. van der Laag, M.D. Snel, P.C.M.M. Magusin, G. de With, Structural, elastic, thermophysical and dielectric properties of zinc aluminate ($ZnAl_2O_4$), J. Eur. Ceram. Soc. 24 (2004) 2417–2424.
[27] I.A. Denisov, Y.V. Volk, A.M. Malyarevich, K.V. Yumashev, O.S. Dymshits, A.A. Zhilin, U. Kang, K.H. Lee, Linear and nonlinear optical properties of cobalt-doped zinc aluminum glass ceramics, J. Appl. Phys. 93 (2003) 3827-3831.
[28] I. Alekseeva, O. Dymshits, V. Ermakov, V. Golubkov, A. Malyarevich, M. Tsenter, A. Zhilin, K. Yumashev, Structure evolution and optical properties of Co-doped zinc aluminosilicate glass-ceramics, Phys. Chem. Glass – Eur. J. Glass Sc. Technol. B 53 (2012) 167-180.
[29] P. Loiko, A. Belyaev, O. Dymshits, I. Evdokimov, V. Vitkin, K. Volkova, M. Tsenter, A. Volokitina, M. Baranov, E. Vilejshikova, A. Baranov, A Zhilin, Synthesis, characterization and absorption saturation of Co:$ZnAl_2O_4$ (gahnite) transparent ceramic and glass-ceramics: A comparative study, J. Alloys Compd. 725 (2017) 998–1005.
[30] A. Goldstein, P. Loiko, Z. Burshtein, N. Skoptsov, I. Glazunov, E. Galun, N. Kuleshov, K. Yumashev, Development of saturable absorbers for laser passive Q-switching near 1.5 μm based on transparent ceramic Co^{2+}:$MgAl_2O_4$, J. Am. Ceram. Soc. 99 (2016) 1324–1331.
[31] W. Luo, Y. Pand, C. Liab, H. Koua, J. Li, Fabrication and spectral properties of hot-pressed Co:$MgAl_2O_4$ transparent ceramics for saturable absorber, J. Alloys Compd. 724 (2017) 45–50.

[32] S. Su, Q. Liu, Z. Hu, X. Chen, H. Pan, X. Liu, L. Wu, J. Li, A simple way to prepare Co:$MgAl_2O_4$ transparent ceramics for saturable absorber, J. Alloys Compd. 797 (2019) 1288-1294.
[33] W. Luo, P. Ma, T. Xie, J. Dai, Y. Pan, H. Kou, J. Li, Fabrication and spectroscopic properties of Co:$MgAl_2O_4$ transparent ceramics by the HIP post-treatment, Opt. Mater. 69 (2017) 152–157.
[34] Q. Liu, S. Su, Z. Hu, X. Chen, T. Xie, Z. Yang, H. Pan, X. Liu, J. Li, Fabrication and properties of Co:$MgAl_2O_4$ transparent ceramics for a saturable absorber from coprecipitated nanopowder, J. Am. Ceram. Soc. 102 (2019) 3097-3102.
[35] S. Su, Q. Liu, Z. Hu, X. Chen, H. Pan, X. Liu, L. Wu, J. Li, A simple way to prepare Co:$MgAl_2O_4$ transparent ceramics for saturable absorber, J. Alloys Compd. 797 (2019) 1288-1294.
[36] A. Goldstein, Y. Yeshurun, M. Vulfson, H. Kravits, Fabrication of transparent polycrystalline $ZnAl_2O_4$ – A new optical bulk ceramic, J. Am. Ceram. Soc. 95 (2012) 879–882.
[37]. B.-N. Kim, K. Hiraga, A. Jeong, C. Hu, T. S. Suzuki, J.-D. Yun, Y. Sakka, Transparent $ZnAl_2O_4$ ceramics fabricated by spark plasma sintering, J. Ceram. Soc. Japan 122 (2014) 784–787.
[38] P. Fu, Z.Y. Wang, Z.D. Lin, Y.Q. Liu, V. A. L. Roy, The microwave dielectric properties of transparent $ZnAl_2O_4$ ceramics fabricated by spark plasma sintering, J. Mater. Sci.: Mater. Electron. 28 (2017) 9589–9595.
[39] X. Yong, F. Ping, Z. Baohua, G. Juan, Z. Lin, W. Xuehua, Optical properties of transparent $ZnAl_2O_4$ ceramics: A new transparent material prepared by spark plasma sintering, Mater. Lett. 123 (2014) 142–144.
[40] M. Sokol, S. Meir, E. Strumza, S. Kalabukhov, S. Hayun, N. Frage, On the effects of LiF on the synthesis and reactive sintering of gahnite, Ceram. Int. 43 (2017) 14891–14896.
[41] C. Yang, W. Zhu, S. Sen, R. H. R. Castro, Site Inversion induces thermodynamic stability against coarsening in zinc aluminate spinel, J. Phys. Chem. C 123 (2019) 8818–8826.
[42] C. Yang, A. Thron, R. H. R. Castro, Grain boundary strengthening in nanocrystalline zinc aluminate, J. Am. Ceram. Soc. 102 (2019) 6904-6912.
[43] V. Elakkiya, S. Sumathi, Ce and Fe doped gahnite: Cost effective solar reflective pigment for cool coating applications, J. Alloys Compd. 820 (2020) 153174.
[44] R. Ianoş, R. Băbuţă, C. Păcurariu, R. Lazău, R. Istratie, C. Butaciu, Combustion synthesis of $ZnAl_2O_4$ powders with tuned surface area, Ceram. Int. 43 (2017) 8975–8981.
[45] R. Ianoş, E. Muntean, C. Păcurariu, R. Lazău, C. Bandas, G. Delinescu, Combustion synthesis of a blue Co-doped zinc aluminate near-infrared reflective pigment, Dyes Pigments, 142 (2017) 24-31.
[46] M. Jain, Manju, A. Gundimeda, A. Kumar, S. Kumar, G. Gupta, Sung Ok Won, K. Hwa Chae, A. Vij, A. Thakura, Enhanced near-infrared luminescence in zinc aluminate bestowed by fuel-blended combustion approach, J. Alloys Compd. 797 (2019) 148-158.

[47] T. C. de S. Santos, D. P. do Rosario, C. M. L. Costa, D. C. Estumano, N. F. da P. Ribeiro, Synthesis and characterization of pigments based on copper-zinc aluminate ($Cu_xZn_{1-x}Al_2O_4$) by combustion, Ceram. Int. 46 (2020) 2332-2343.
[48] T. C. de S. Santos, A. C. M. Almeida, D. do R. Pinheiro, C. M. L. Costa, D. C. Estumano, N. F. da P. Ribeiro, Synthesis and characterization of colourful aluminates based on nickel and zinc, J. Alloys Compd. 815 (2020) 152477.
[49] A.V. Belyaev, M.I. Lelet, N.I. Kirillova, N.M. Khamaletdinova, M.S. Boldin, A.A. Murashov, S.S. Balabanov, Sol-gel synthesis and characterization of $ZnAl_2O_4$ powders for transparent ceramics, Ceram. Int. 45 (2019) 4835–4839.
[50] D. Dollimore, K.H. Tonge, The thermal decomposition of zinc and manganous formats, J. Inorg. Nucl. Chem. 29 (1967) 621– 627.
[51] A.V. Belyaev, I.I. Evdokimov, V.V. Drobotenko, A.A. Sorokin, A new approach to producing transparent $ZnAl_2O_4$ ceramics, J. Eur. Ceram. Soc. 37 (2017) 2747–275.
[52] B. Brunetti, D. Lelo, V. Piacente, P. Scardala, Vapor pressures and sublimation enthalpies of cadmium difluoride and zinc difluoride by the torsion-effusion method, J. Chem. Eng. Data 53 (2008) 2101–2105.
[53] R.M. Biefeld, H.A. Eick, The sublimation thermodynamics of zinc (II) fluoride, J. Chem. Thermodyn. 5 (1973) 353–360.
[54] H. Lipson, H. Steeple, in: McMillan (Ed.), Interpretation of X-ray powder patterns, Martins Press, London, N.Y., 1970, 344 p.
[55] R.F. Cooley, J.S. Reed. Equilibrium cation distribution in $NiAl_2O_4$, $CuAl_2O_4$, and $ZnAl_2O_4$ spinels, J. Amer. Ceram. Soc. 55 (1972) 395-398.
[56] W.B. White, B.A. DeAngelis, Interpretation of the vibrational spectra of spinels, Spectrochim. Acta 23A (1967) 985-995.
[57] S. Lopez-Moreno, P. Rodriguez-Hernandez, A. Munoz, A.H. Romero, F.J. Manjon, D. Errandonea, E. Rusu, V.V. Ursaki, Lattice dynamics of $ZnAl_2O_4$ and $ZnGa_2O_4$ under high pressure, Ann. Phys. 523 (2011) 157-167.
[58] R.M. Macfarlane, S. Ushioda, Light scattering from phonons in CoF_2, Solid State Commun. (1970) 1081-1083.
[59] S.P.S. Porto, P.A. Fleury, T.C. Damen, Raman spectra of TiO_2, MgF_2, ZnF_2, FeF_2, and MnF_2, Phys. Rev. 154 (1967) 522-526
[60] R. Cuscó, E. Alarcón-Lladó, J. Ibáñez, L. Artús, J. Jiménez, B. Wang, M.J. Callahan, Temperature dependence of Raman scattering in ZnO, Phys. Rev. B 75 (2007) 165202.
[61] O. Medenbach, T. Siritanon, M.A. Subramanian, R.D. Shannon, R.X. Fischer, G.R. Rossman, Refractive index and optical dispersion of In_2O_3, $InBO_3$ and gahnite, Mater. Res. Bull. 48 (2013) 2240-2243.
[62] K. Tanaka, T. Mukai, T. Ishihara, K. Hirao, N. Soga, S. Sogo, M. Ashida, R. Kato, Preparation and optical properties of transparent glass-ceramics containing cobalt (II) ions, J. Amer. Ceram. Soc. 76 (1993) 2839-2845.

[63] M. Ardit, G. Cruciani, M. Dondi, Structural relaxation in tetrahedrally coordinated Co^{2+} along the gahnite-Co-aluminate spinel solid solution, Amer. Mineralog. 97 (2012) 1394-1401.
[64] X. Duan, D. Yuan, F. Yu, Cation distribution in Co-doped $ZnAl_2O_4$ nanoparticles studied by X-ray photoelectron spectroscopy and ^{27}Al solid-state NMR spectroscopy, Inorg. Chem. 50 (2011) 5460-5467.
[65] Y. Tanabe, S. Sugano, On the absorption spectra of complex ions I, J. Phys. Soc. Jap. 9 (1954) 753–766.
[66] P.J. Deren, W. Strek, B. Jezowska-Trzebiatowska, I. Trabjerg, The optical spectra of Co^{2+} in $MgAl_2O_4$ spinel, J. Phys. IV 1 (1991) C7-279–C7-283.
[67] J. Popović, E. Tkalčec, B. Gržeta, S. Kurajica, B. Rakvin, Inverse spinel structure of Co-doped gahnite, Amer. Mineralog. 94 (2009) 771-776.
[68] H.S.C. O'Neill, W.A. Dollase, Crystal structures and cation distributions in simple spinels from powder XRD structural refinements: $MgCr_2O_4$, $ZnCr_2O_4$, Fe_3O_4 and the temperature dependence of the cation distribution in $ZnAl_2O_4$, Phys. Chem. Mineral. 20 (1994) 541-555.
[69] R.D. Shannon, Revised effective ionic radii and systematic studies of interatomic distances in halides and chalcogenides, Acta Crystallogr. 32 (1976) 751-767.
[70] B. Brunetti, V. Piacente, Torsion and Knudsen measurements of cobalt and nickel difluorides and their standard sublimation enthalpies, J. Alloys Compd. 236 (1996) 63-69.
[71] W. P. Witt, R. F. Barrow, The heat of sublimation of aluminium trifluoride and the heat of formation of aluminium monofluoride, Trans. Faraday Soc. 55 (1959) 730-735.
[72] L. Esposito, A. Piancastelli, P. Miceli, S. Martelli, A thermodynamic approach to obtaining transparent spinel ($MgAl_2O_4$) by hot pressing, J. Eur. Ceram. Soc. 35 (2015) 651–661.
[73] Q. Chen, Z. Fang, H. Song, F. Zhang, J. Nie, Z. Chen, Y. Dai, J. Qiu, Femtosecond laser induced space-selective precipitation of Cr^{3+}-doped $ZnAl_2O_4$ crystal in glass, J. Alloys Compd. 699 (2017) 243-246.
[74] J. Derkosch, W. Mikenda, A. Preisinger, N-lines and chromium-pairs in the luminescence spectra of the spinels $ZnAl_2O_4$: Cr^{3+} and $MgAl_2O_4$:Cr^{3+}, J. Sol. State Chem. 22 (1977) 127-133.
[75] M. Jain, A. Gundimeda, S. Kumar, G. Gupta, S.O. Won, K.H. Chae, A. Vij, A. Thakur, Defect induced broadband visible to near-infrared luminescence in $ZnAl_2O_4$ nanocrystals, Appl. Surf. Sci. 480 (2019) 945-950.
[76] M. Jain, A. Gundimeda, A. Kumar, S. Kumar, G. Gupta, S.O. Won, K.H. Chae, A. Vij, A. Thakur, Enhanced near-infrared luminescence in zinc aluminate bestowed by fuel-blended combustion approach, J. Alloys Compd. 797 (2019) 148-158.
[77] A.T. Khalil, M. Ovais, I. Ullah, M. Ali, Z.K. Shinwari, M. Maaza, Biosynthesis of iron oxide (Fe_2O_3) nanoparticles via aqueous extracts of *Sageretia thea* (Osbeck.) and their pharmacognostic properties, Green Chem. Lett. Rev. 10 (2017) 186-201.

[78] N. Matinise, K. Kaviyarasu, N. Mongwaketsi, S. Khamlich, L. Kotsedi, N. Mayedwa, M. Maaza, Green synthesis of novel zinc iron oxide ($ZnFe_2O_4$) nanocomposite via Moringa Oleifera natural extract for electrochemical applications, Appl. Surf. Sci. 446 (2018) 66-73.

List of figure captions

Fig. 1. Thermal evolution of the 0.1 at.% Co:$ZnAl_2O_4$ / 6 wt% ZnF_2 precursor: thermal gravimetric analysis (TGA) mass loss curve (*black*) and differential thermal analysis (DTA) curve (*blue*) measured under heating in air.

Fig. 2. X-ray diffraction (XRD) patterns of the powders doped with 0.1 at.% Co and 6 wt% ZnF_2 annealed at 300, 500, 700 and 900 °C. *Circles* indicate the diffraction peaks of $ZnAl_2O_4$, *asterisks* – ZnO.

Fig. 3. Photographs of transparent ceramics sintered at 1520 °C for 4 h from 0.02 at.% Co (*upper raw*) and 0.1 at.% Co (*lower raw*) doped $ZnAl_2O_4$ powders with 3, 6 or 10 wt% ZnF_2.

Fig. 4. X-ray powder diffraction (XRD) patterns of ceramic samples prepared from powders containing 0.1 at.% Co and 3 / 10 wt% ZnF_2, *numbers* denote the Miller's indices (*hkl*), *red peaks* – diffraction peaks for undoped $ZnAl_2O_4$ (ICSD card #9559).

Fig. 5. Scanning Electron Microscope (SEM) images of a fracture surface of ceramics produced from powders containing 0.1 at.% Co and (a) 3 wt% ZnF_2 and (b) 10 wt% ZnF_2.

Fig. 6. (a) Grain size distribution for ceramics produced from powders containing 0.02 at.% Co and 3, 6 or 10 wt% ZnF_2; (b) Mean grain size *vs*. the ZnF_2 concentration in the precursor powders.

Fig. 7. EDX spectra for ceramics prepared from powders containing 0.1 at.% Co and 3-10 wt% ZnF_2.

Fig. 8. EDX mapping for ceramics prepared from powders containing 0.1 at.% Co and 10 wt% ZnF_2: (a) SEM image of the fracture surface, (c-f) the corresponding element maps: (b) Al, (c) O, (d) Zn, (e) F and (f) Co.

Fig. 9. Raman spectra of Co:$ZnAl_2O_4$ transparent ceramics (the spectra are shifted for the sake of comparison), λ_{exc} = 514 nm.

Fig. 10. In-line transmission spectra of laser-grade polished Co:$ZnAl_2O_4$ ceramic disks (thickness: 2 mm): (a) transmission of as-sintered samples; (b) effect of annealing on transmission in the UV and visible of ceramics prepared from powders doped with 0.1 at.% Co and 3 wt% ZnF_2. *Numbers* in (b) indicate the peak wavelengths.

Fig. 11. (a) Tanabe-Sugano diagram of energy levels of d^7 tetrahedral complexes (for C/B = 4.50), *vertical dashed line* marks the case of Co^{2+}:$ZnAl_2O_4$; (b) crystal-field splitting of Co^{2+} ions in $ZnAl_2O_4$ and $MgAl_2O_4$ crystals (after [25,65]). *Green arrows* indicate the observed transitions in emission.

Fig. 12. Analysis of the $^4A_2(^4F) \rightarrow {}^4T_1(^4F)$ absorption transition of Co^{2+} ions in T_d sites in Co:$ZnAl_2O_4$ ceramics: (a) absorption spectra; (b) variation of absorption coefficient α_{abs} at ~1.54 μm with the ZnF_2 concentration in the precursor: *dashed line*s – expected absorption calculated from the GSA cross-section and the nominal Co^{2+} concentration.

Fig. 13. Luminescence of Co:$ZnAl_2O_4$ transparent ceramics: (a) spectra of non-annealed samples; (b) effect of annealing on the luminescence spectra of ceramics prepared from powders doped with 0.02 / 0.1 at.% Co and 3 wt% ZnF_2; (c) details of impurity and defect emissions for ceramics prepared from powders doped with 0.02 at.% Co and 3 wt% ZnF_2, *numbers* indicate the peak wavelengths. λ_{exc} = 514 nm.

Fig. 14. Luminescence decay curves of Co:$ZnAl_2O_4$ transparent ceramics prepared from powders doped with 0.1 at.% Co and 3–10 wt% ZnF_2 (semi-log plots): *circles* – experimental data, *solid lines* – their single-exponential fits, τ_{slow} – luminescence lifetime. λ_{exc} = 405 nm (ps pulses), λ_{lum} ~ 650 nm.

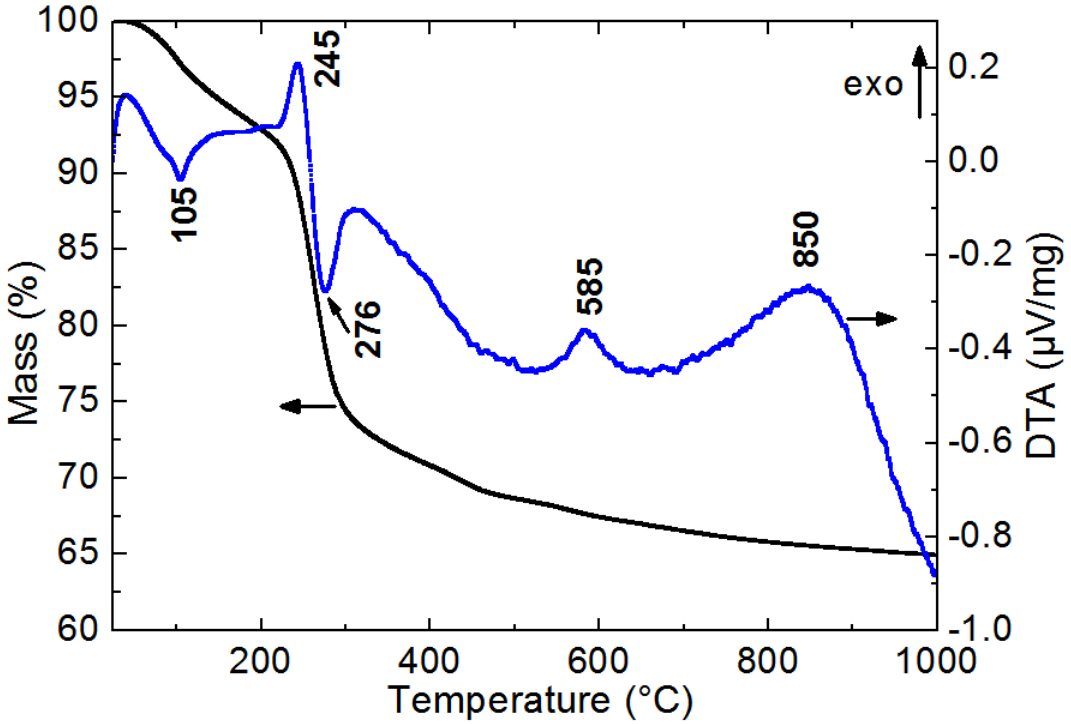
Mass (%)
DTA (μV/mg)
Temperature (°C)
exo
105
245
276
585
850

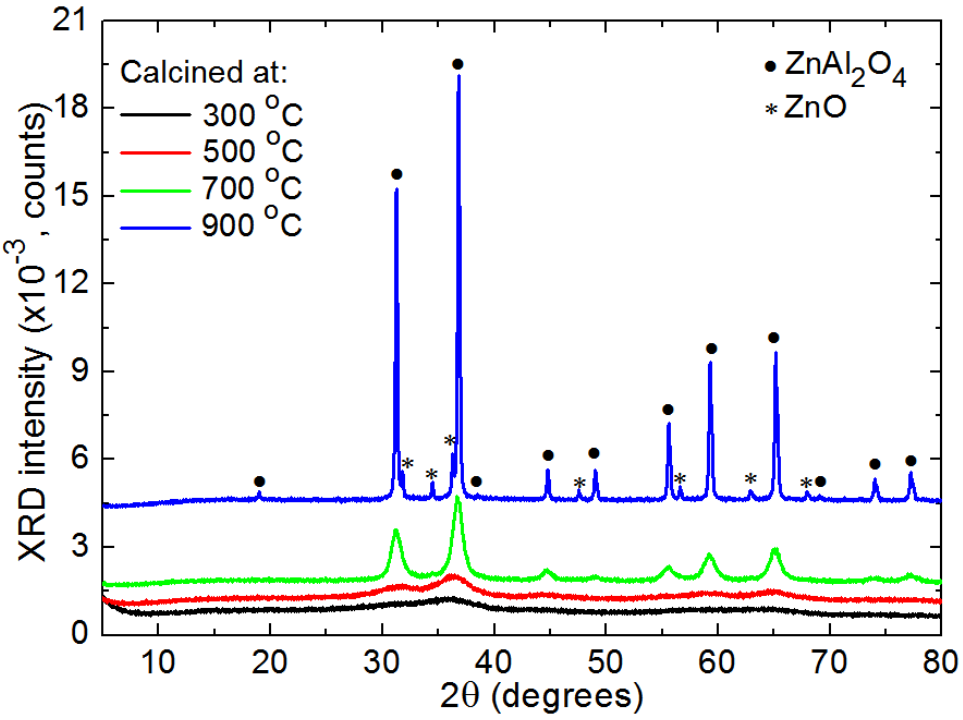
Calcined at:
300 °C
500 °C
700 °C
900 °C
ZnAl2O4
ZnO
XRD intensity (x10-3, counts)
2θ (degrees)

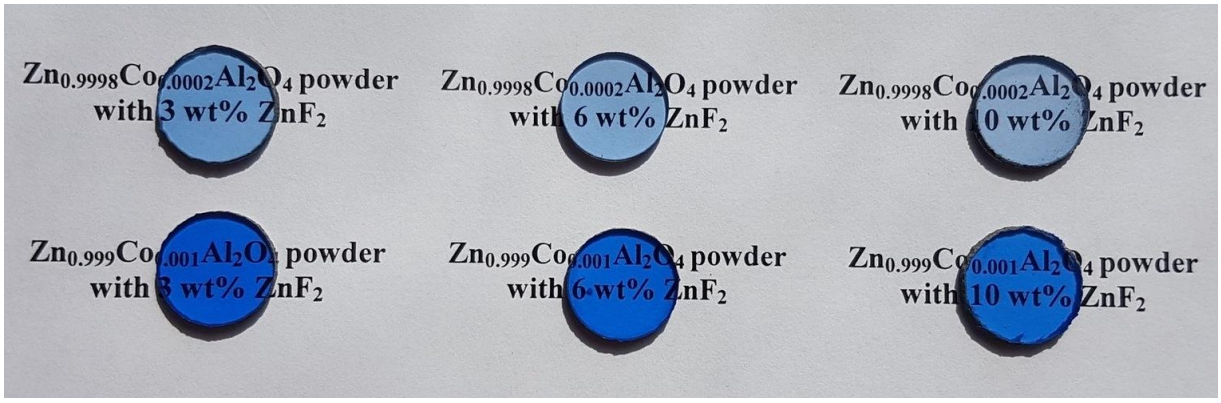
$Zn_{0.9998}Co_{0.0002}Al_2O_4$ powder with 3 wt% ZnF_2
$Zn_{0.9998}Co_{0.0002}Al_2O_4$ powder with 6 wt% ZnF_2
$Zn_{0.9998}Co_{0.0002}Al_2O_4$ powder with 10 wt% ZnF_2
$Zn_{0.999}Co_{0.001}Al_2O_4$ powder with 3 wt% ZnF_2
$Zn_{0.999}Co_{0.001}Al_2O_4$ powder with 6 wt% ZnF_2
$Zn_{0.999}Co_{0.001}Al_2O_4$ powder with 10 wt% ZnF_2

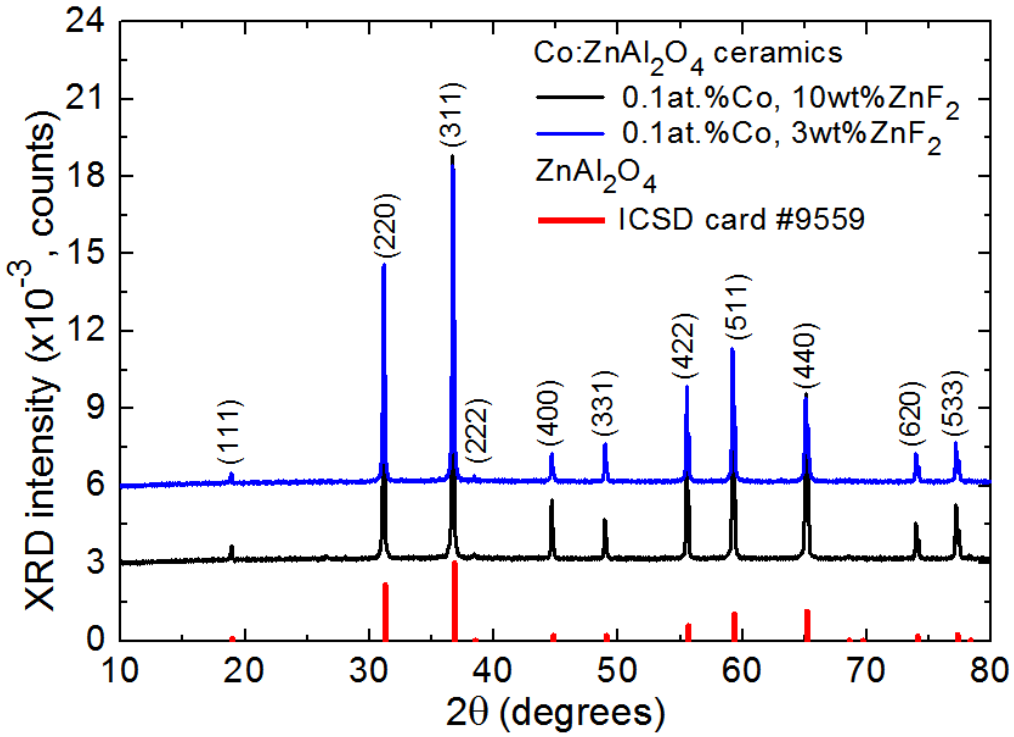
Co:$ZnAl_2O_4$ ceramics
0.1at.%Co, 10wt%ZnF_2
0.1at.%Co, 3wt%ZnF_2
$ZnAl_2O_4$
ICSD card #9559
XRD intensity (x10^{-3}, counts)
2θ (degrees)
(111)
(220)
(311)
(222)
(400)
(331)
(422)
(511)
(440)
(620)
(533)

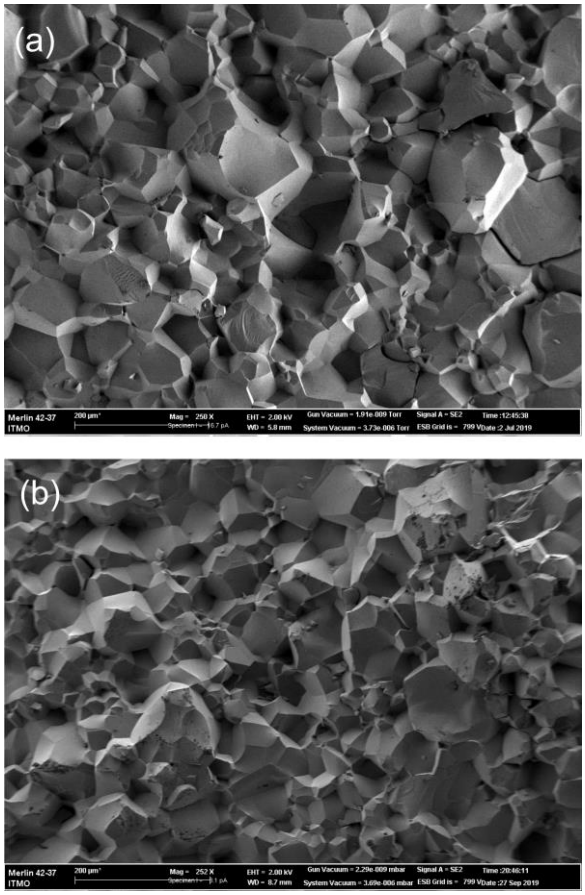
(a)
(b)

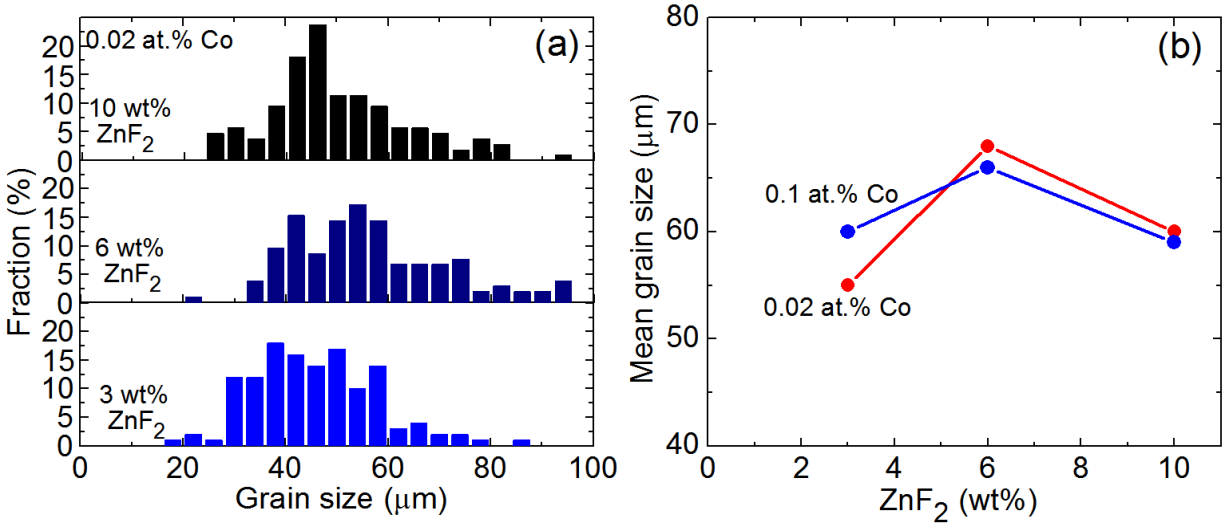
0.02 at.% Co
10 wt% ZnF2
6 wt% ZnF2
3 wt% ZnF2
(a)
Fraction (%)
Grain size (μm)
(b)
0.1 at.% Co
0.02 at.% Co
Mean grain size (μm)
ZnF2 (wt%)

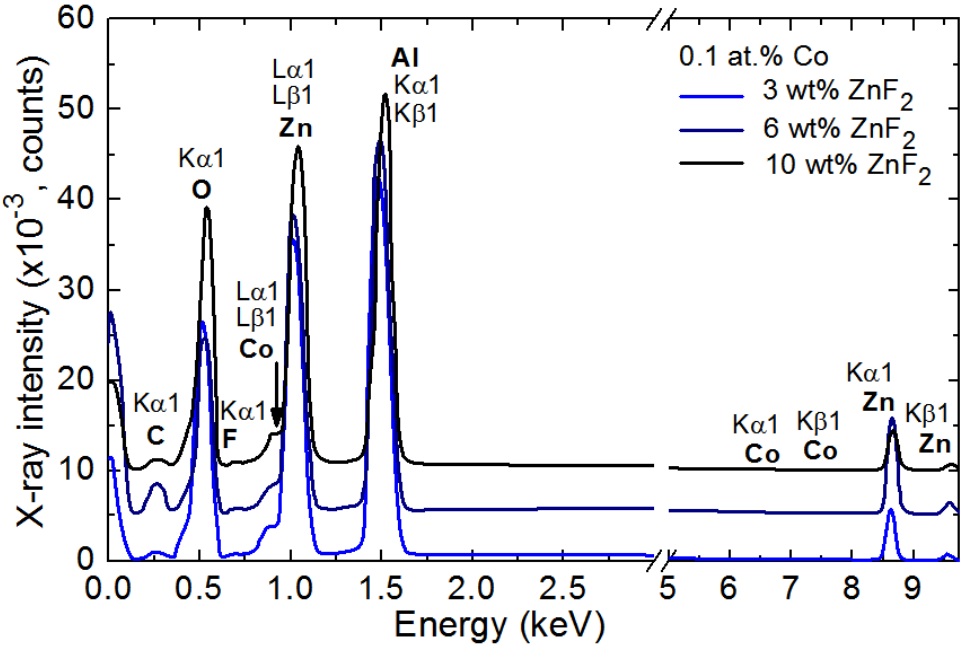
X-ray intensity (x10-3, counts)
Energy (keV)
0.1 at.% Co
3 wt% ZnF2
6 wt% ZnF2
10 wt% ZnF2
Kα1 C
Kα1 O
Lα1 Lβ1 Zn
Kα1 F
Lα1 Lβ1 Co
Al Kα1 Kβ1
Kα1 Co
Kβ1 Co
Kα1 Zn
Kβ1 Zn

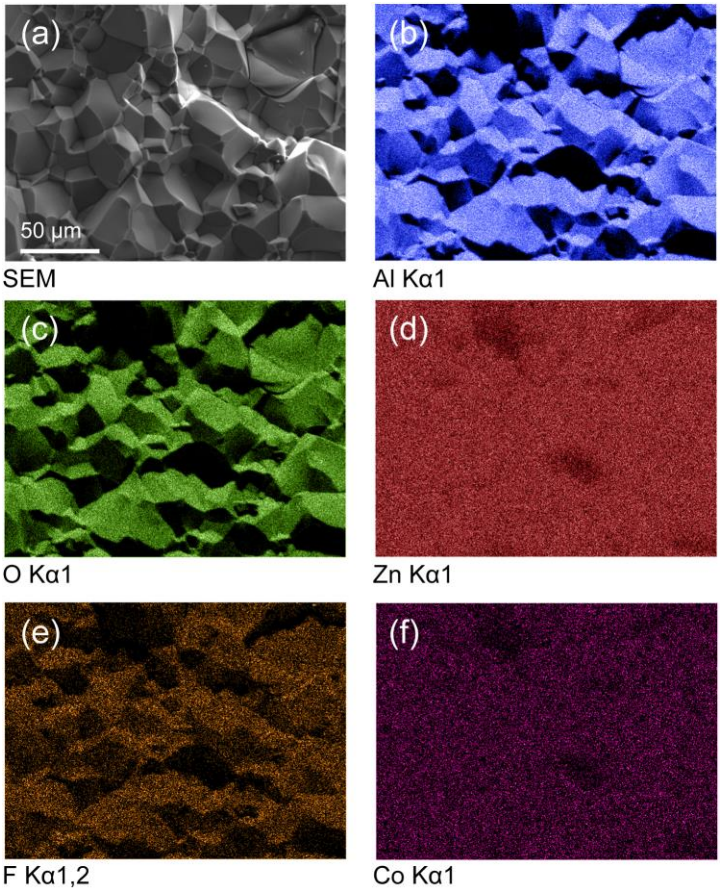
(a)
50 μm
SEM
(b)
Al Kα1
(c)
O Kα1
(d)
Zn Kα1
(e)
F Kα1,2
(f)
Co Kα1

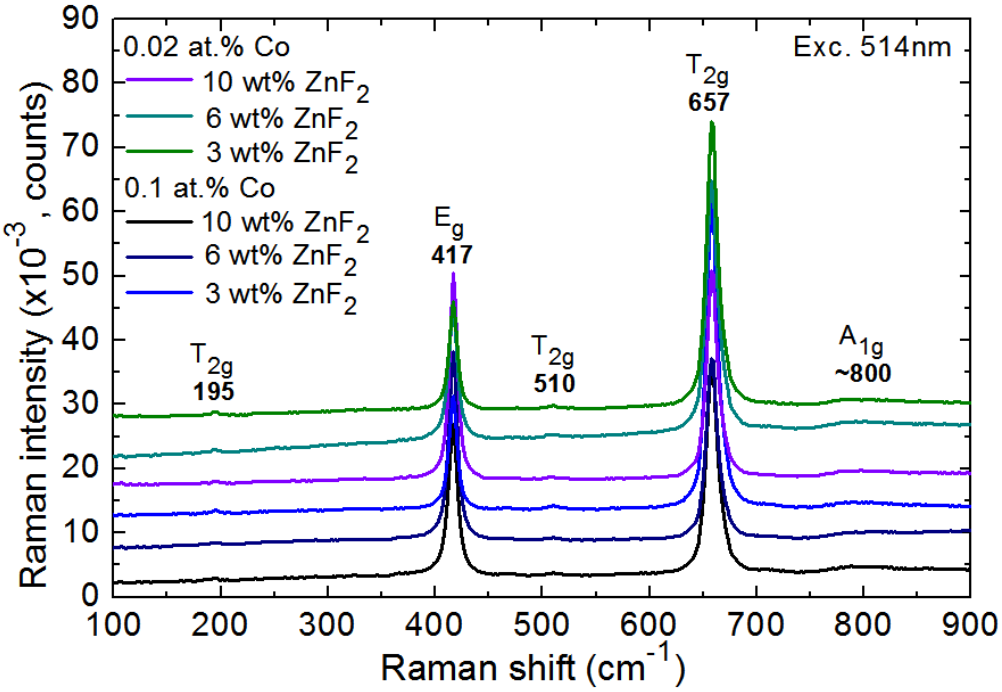
0.02 at.% Co
10 wt% ZnF2
6 wt% ZnF2
3 wt% ZnF2
0.1 at.% Co
10 wt% ZnF2
6 wt% ZnF2
3 wt% ZnF2
Exc. 514nm
T2g
195
Eg
417
T2g
510
T2g
657
A1g
~800
Raman intensity (x10-3, counts)
Raman shift (cm-1)
0
10
20
30
40
50
60
70
80
90
100
200
300
400
500
600
700
800
900

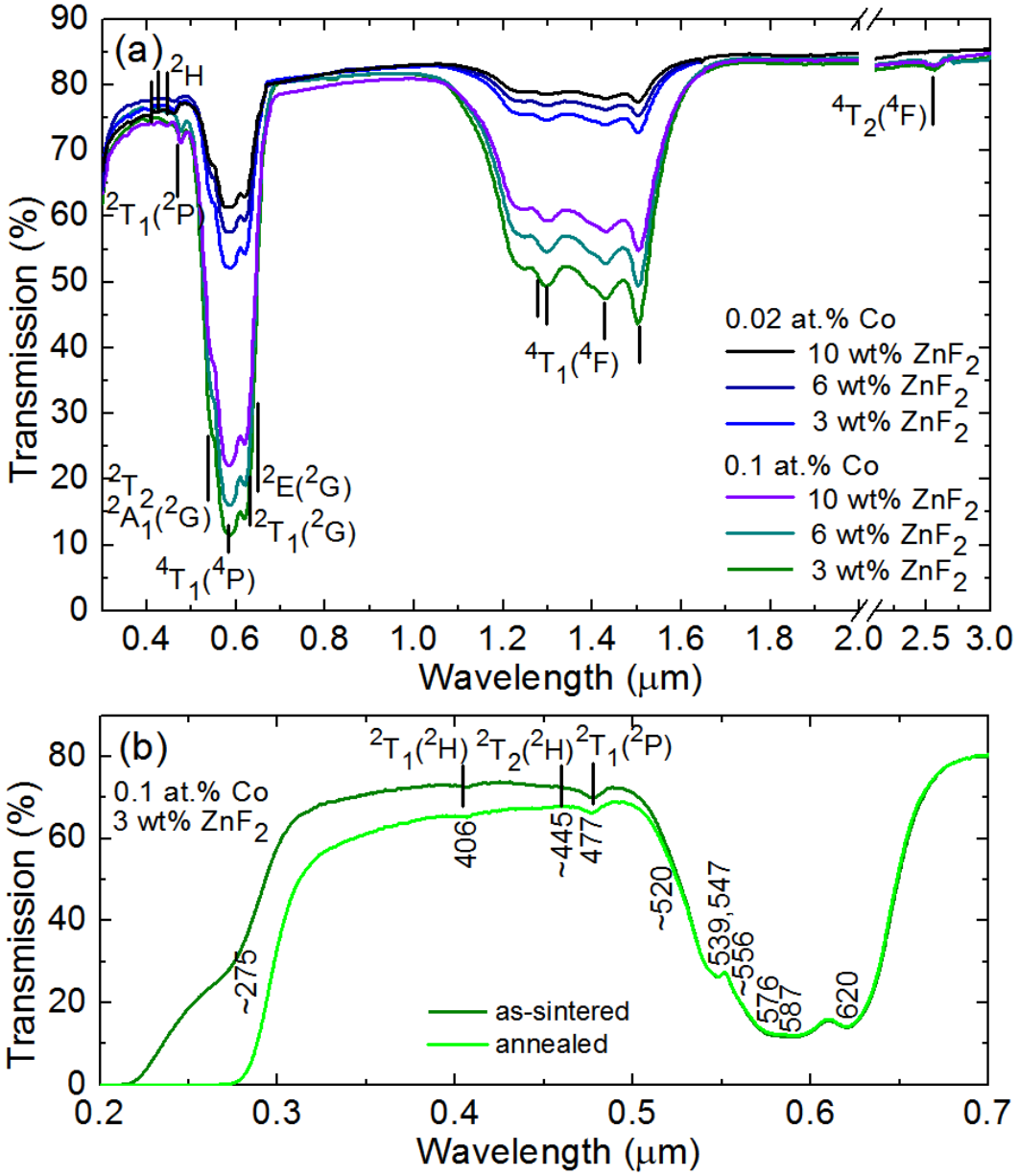
(a)
Transmission (%)
Wavelength (μm)
^2H
$^2T_1(^2P)$
$^2T_2$
$^2A_1(^2G)$
$^2E(^2G)$
$^2T_1(^2G)$
$^4T_1(^4P)$
$^4T_1(^4F)$
$^4T_2(^4F)$
0.02 at.% Co
10 wt% ZnF_2
6 wt% ZnF_2
3 wt% ZnF_2
0.1 at.% Co
10 wt% ZnF_2
6 wt% ZnF_2
3 wt% ZnF_2
(b)
0.1 at.% Co
3 wt% ZnF_2
$^2T_1(^2H)$ $^2T_2(^2H)$ $^2T_1(^2P)$
~275
406
~445
477
~520
539,547
~556
576
587
620
as-sintered
annealed
Transmission (%)
Wavelength (μm)

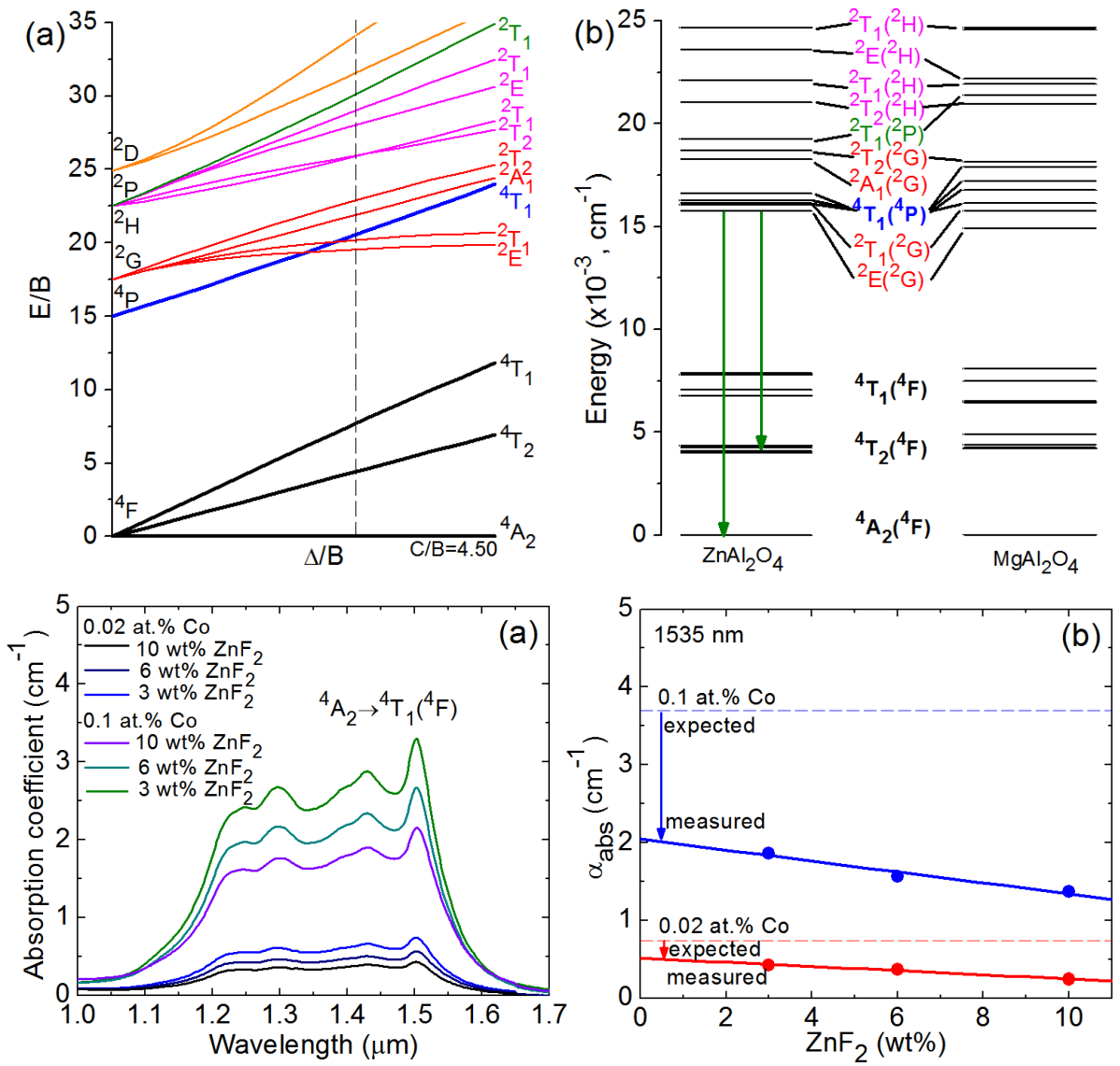
(a)
E/B
Δ/B
C/B=4.50
^2D
^2P
^2H
^2G
^4P
^4F
$^2T_1$
$^2T_1$
^2E
$^2T_1$
$^2T_2$
$^2T_2$
$^2A_1$
$^4T_1$
$^2T_1$
^2E
$^4T_1$
$^4T_2$
$^4A_2$
(b)
Energy (x10^{-3}, cm^{-1})
$^2T_1(^2H)$
$^2E(^2H)$
$^2T_1(^2H)$
$^2T_2(^2H)$
$^2T_1(^2P)$
$^2T_2(^2G)$
$^2A_1(^2G)$
$^4T_1(^4P)$
$^2T_1(^2G)$
$^2E(^2G)$
$^4T_1(^4F)$
$^4T_2(^4F)$
$^4A_2(^4F)$
$ZnAl_2O_4$
$MgAl_2O_4$
(a)
Absorption coefficient (cm^{-1})
Wavelength (μm)
0.02 at.% Co
10 wt% ZnF_2
6 wt% ZnF_2
3 wt% ZnF_2
0.1 at.% Co
10 wt% ZnF_2
6 wt% ZnF_2
3 wt% ZnF_2
$^4A_2 \rightarrow {}^4T_1(^4F)$
(b)
1535 nm
α_{abs} (cm^{-1})
ZnF_2 (wt%)
0.1 at.% Co
expected
measured
0.02 at.% Co
expected
measured

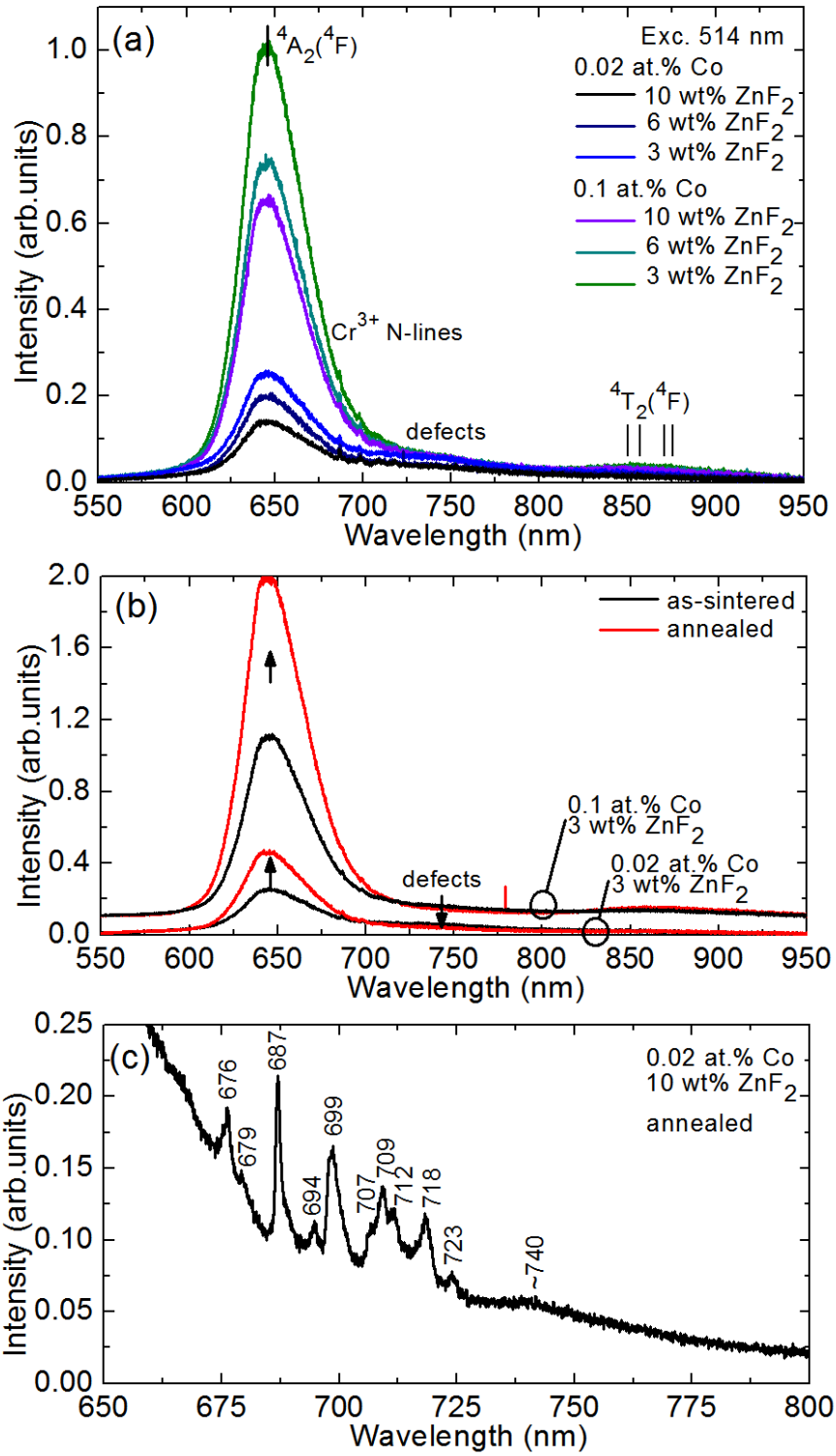
(a)
Exc. 514 nm
0.02 at.% Co
10 wt% ZnF2
6 wt% ZnF2
3 wt% ZnF2
0.1 at.% Co
10 wt% ZnF2
6 wt% ZnF2
3 wt% ZnF2
4A2(4F)
Cr3+ N-lines
defects
4T2(4F)
Intensity (arb.units)
Wavelength (nm)
(b)
as-sintered
annealed
0.1 at.% Co
3 wt% ZnF2
0.02 at.% Co
3 wt% ZnF2
defects
Intensity (arb.units)
Wavelength (nm)
(c)
0.02 at.% Co
10 wt% ZnF2
annealed
676
679
687
694
699
707
709
712
718
723
~740
Intensity (arb.units)
Wavelength (nm)

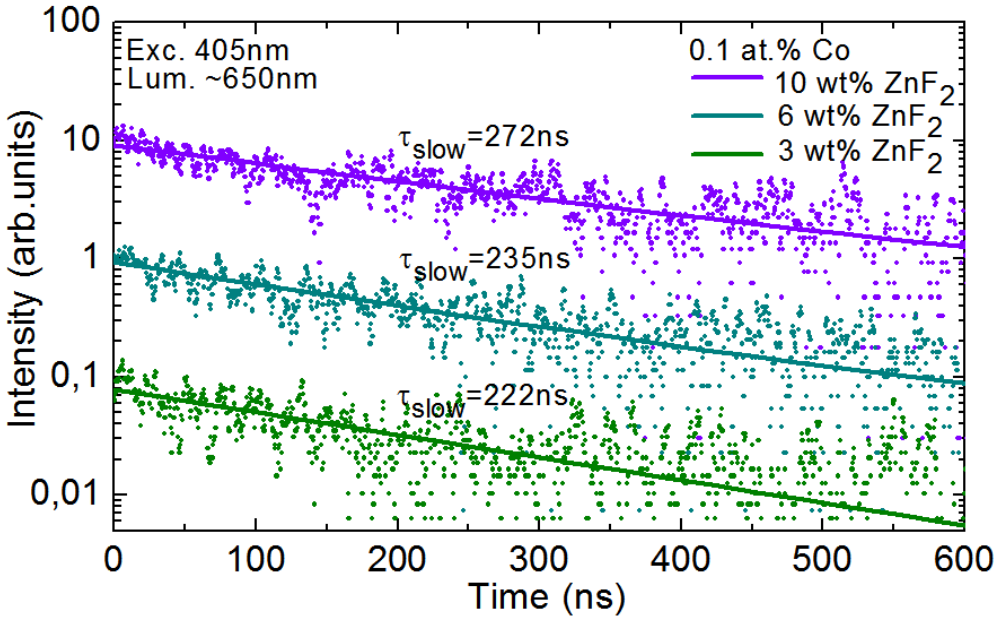

Table 1. Concentration of Co^{2+} ions in tetrahedral (T_d) sites in Co:$ZnAl_2O_4$ initial powders and transparent ceramics (determined from the spectroscopic data).

Material	ZnF_2, wt%	Content of Co^{2+} in T_d sites, at.% (cm^{-3})	
Initial powders	3–10	0.02 (0.303×10^{19})	0.10 (1.514×10^{19})
Ceramics	3	0.011 (0.17×10^{19})	0.050 (0.76×10^{19})
	6	0.010 (0.15×10^{19})	0.052 (0.64×10^{19})
	10	0.007 (0.10×10^{19})	0.037 (0.56×10^{18})